Supporting Information:

Polarization control with plasmonic antenna-tips: A universal approach for optical nano-crystallography and vector-field imaging

Kyoung-Duck Park[1,2] and Markus B. Raschke[*1,2]

[1]*Department of Physics, Department of Chemistry, and JILA, University of Colorado, Boulder, CO, 80309, USA*

[2]*Center for Experiments on Quantum Materials, University of Colorado, Boulder, CO, 80309, USA*

Email: markus.raschke@colorado.edu
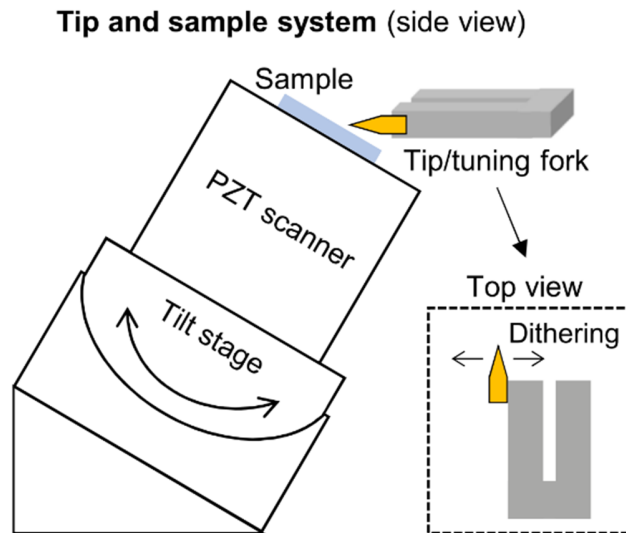
Schematic of tip and sample system

Figure S1: The etched Au tip is glued parallel with the tuning fork. The sample mount on the PZT scanner can be tilted by variable angle with respect to the tip axis by using a tilt stage as shown in Figure. The Au tip is dithering parallel with the sample surface for shear-force tip - sample distance control.

Finite-difference time-domain simulation of the local optical field of a conventional surface normal oriented Au tip
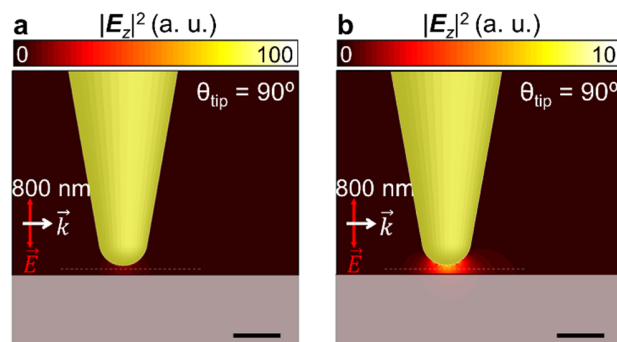

Figure S2: Simulated *out-of-plane* electric field intensity ($|E_z|^2$) map for the surface normal oriented tip near the SiO_2 substrate with excitation wavelength of 800 nm. (a) is the same image as Figure 2c in the main text. (b) is the same data as (a) with different intensity scale bar.

Finite-difference time-domain simulation of the local optical field of tilted Au tip
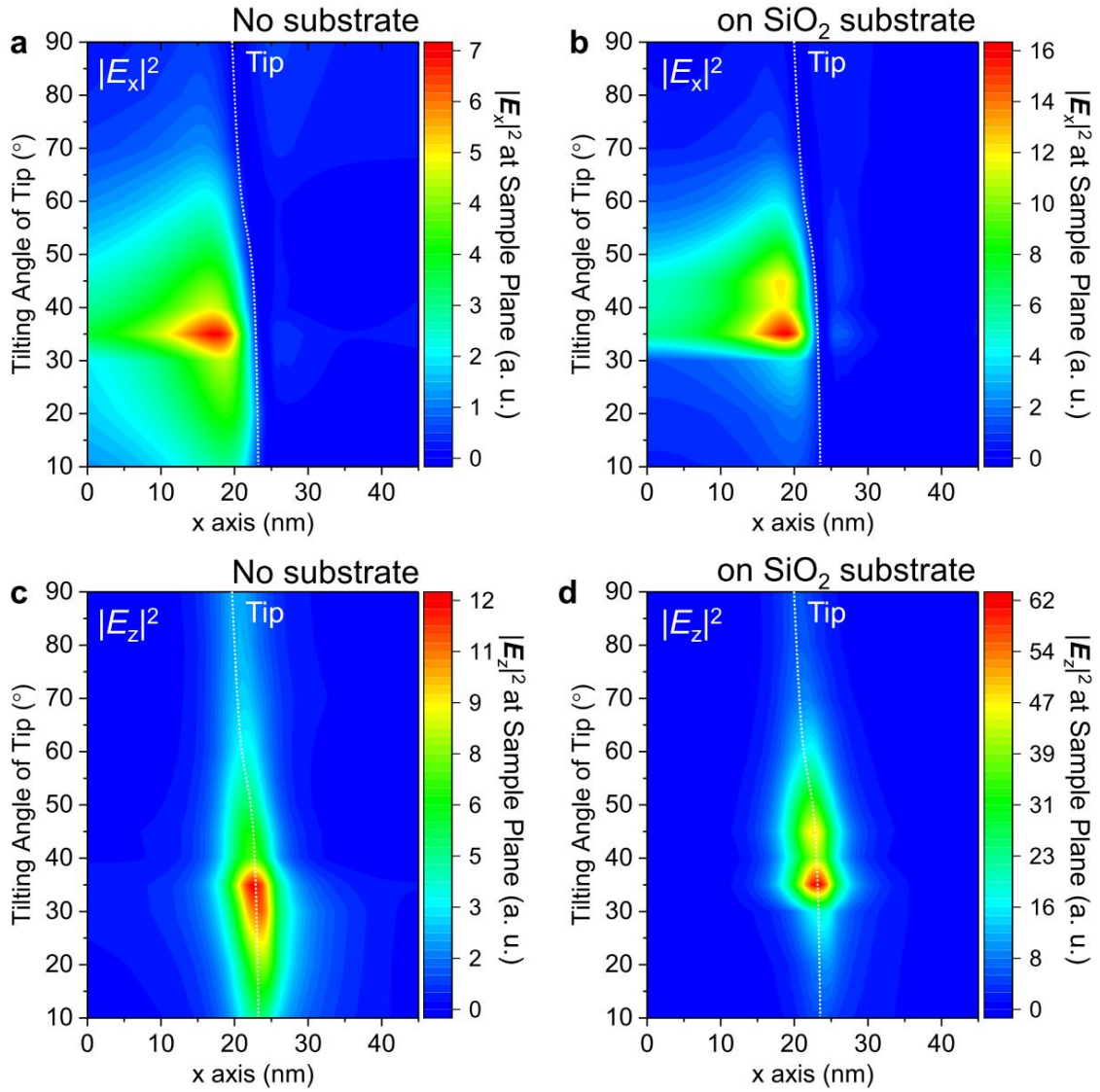

Figure S3: Simulated optical field intensity profiles at the sample plane with respect to the tip tilt angle. $|E_x|^2$ (a) and $|E_z|^2$ (c) for the free standing tip (without substrate). $|E_x|^2$ (b) and $|E_z|^2$ (d) for the tip with SiO_2 substrate.
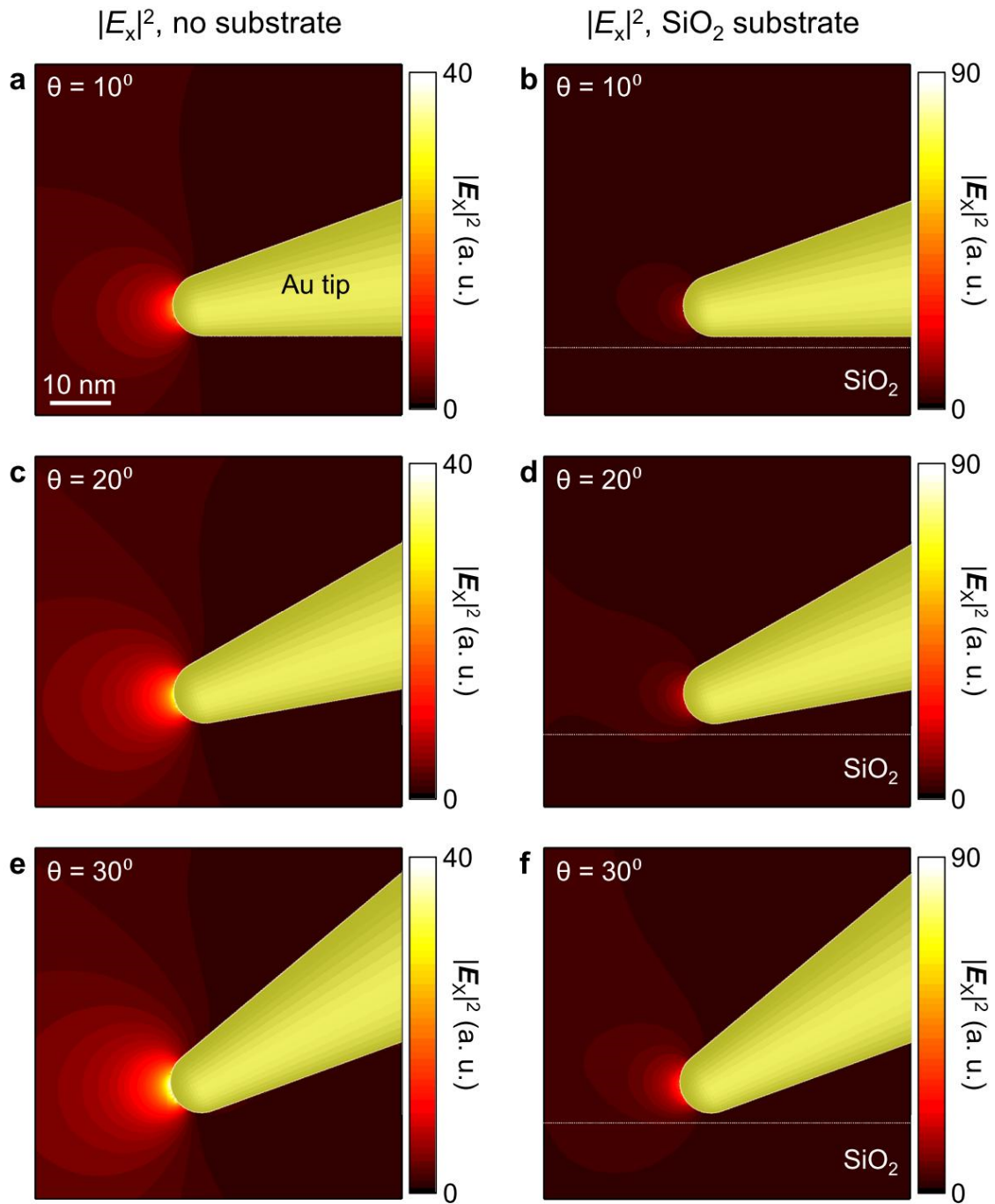
Figure S4: Simulated *in-plane* optical field intensity ($|E_x|^2$) maps with respect to the tip tilt angle. (a, c, e) $|E_x|^2$ for the free standing tip (without substrate). (b, d, f) $|E_x|^2$ for the tip near the SiO₂ substrate.

|E_x|^2, no substrate

|E_x|^2, SiO$_2$ substrate

a θ = 35^0

b θ = 35^0

SiO$_2$

c θ = 40^0

d θ = 40^0

SiO$_2$

e θ = 45^0

f θ = 45^0

SiO$_2$

Figure S5: Simulated *in-plane* optical field intensity (|E_x|^2) maps with respect to the tip tilt angle. (a, c, e) |E_x|^2 for the free standing tip (without substrate). (b, d, f) |E_x|^2 for the tip near the SiO$_2$ substrate.

$|E_x|^2$, no substrate

$|E_x|^2$, SiO$_2$ substrate

Figure S6: Simulated *in-plane* optical field intensity ($|E_x|^2$) maps with respect to the tip tilt angle. (a, c, e) $|E_x|^2$ for the free standing tip (without substrate). (b, d, f) $|E_x|^2$ for the tip near the SiO$_2$ substrate.
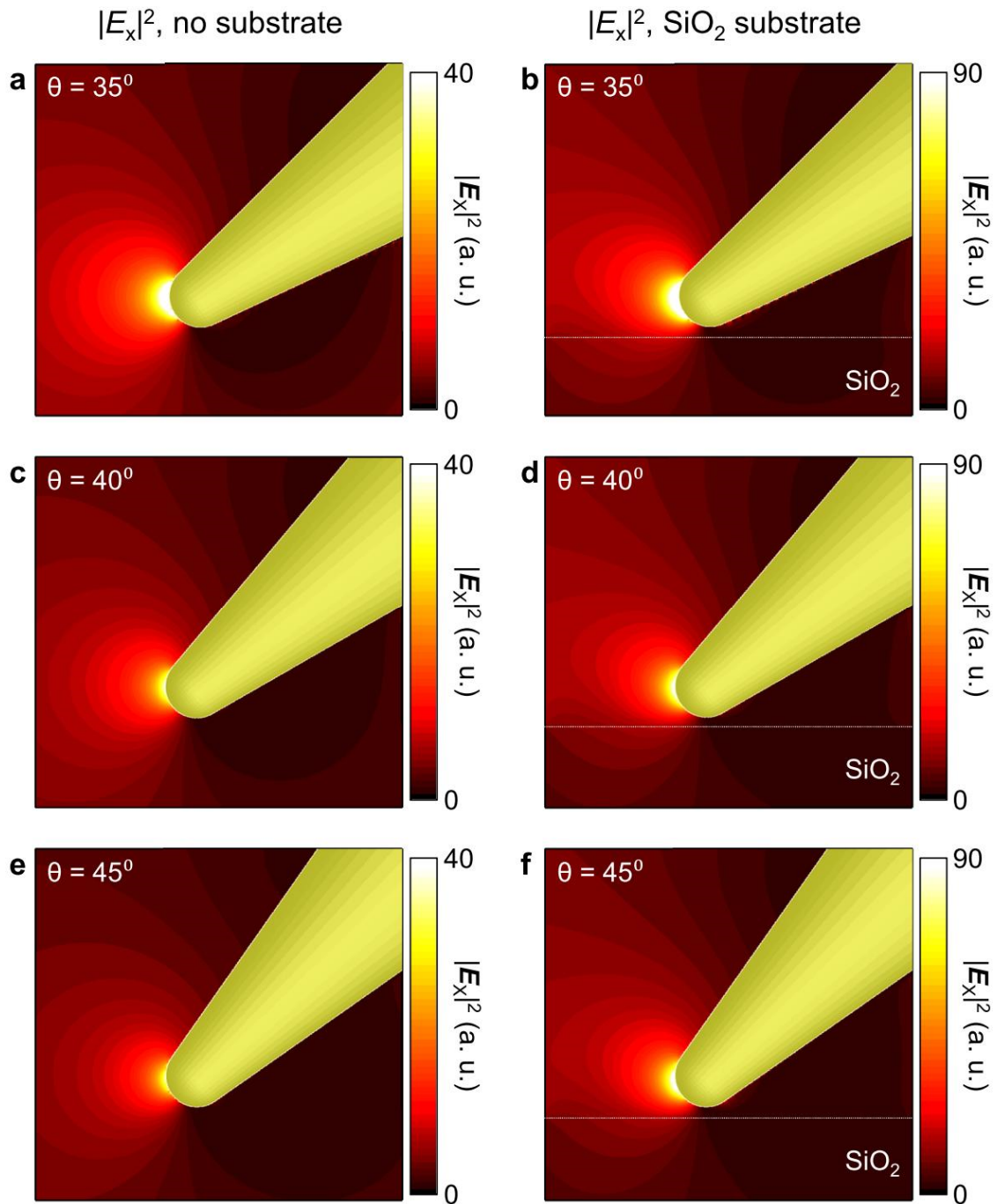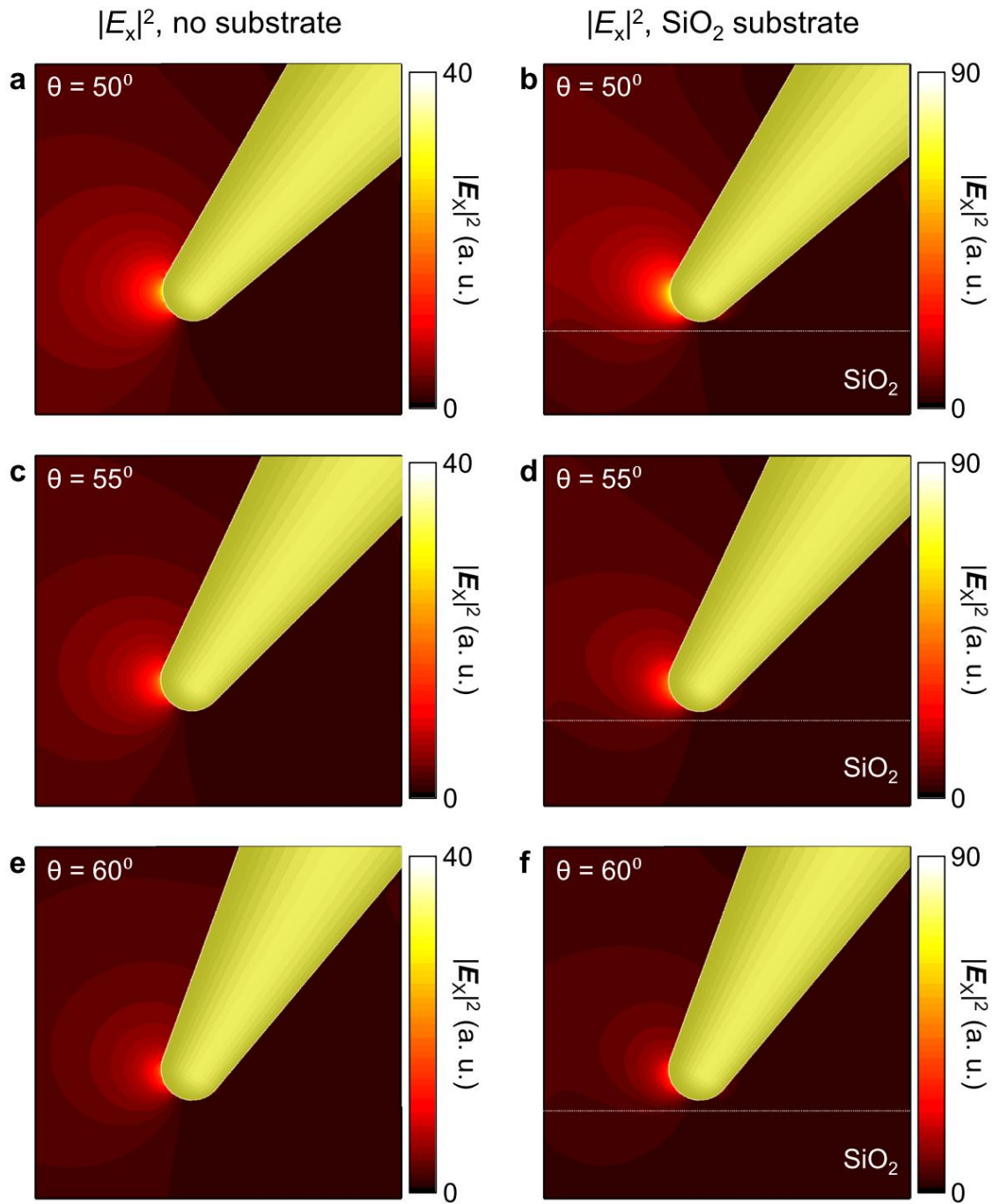
|Ex|², no substrate

a θ = 70⁰ ... 40 ... 0

c θ = 80⁰ ... 40 ... 0

e θ = 90⁰ ... 40 ... 0

|Ex|², SiO₂ substrate

b θ = 70⁰ ... 90 ... SiO₂ ... 0

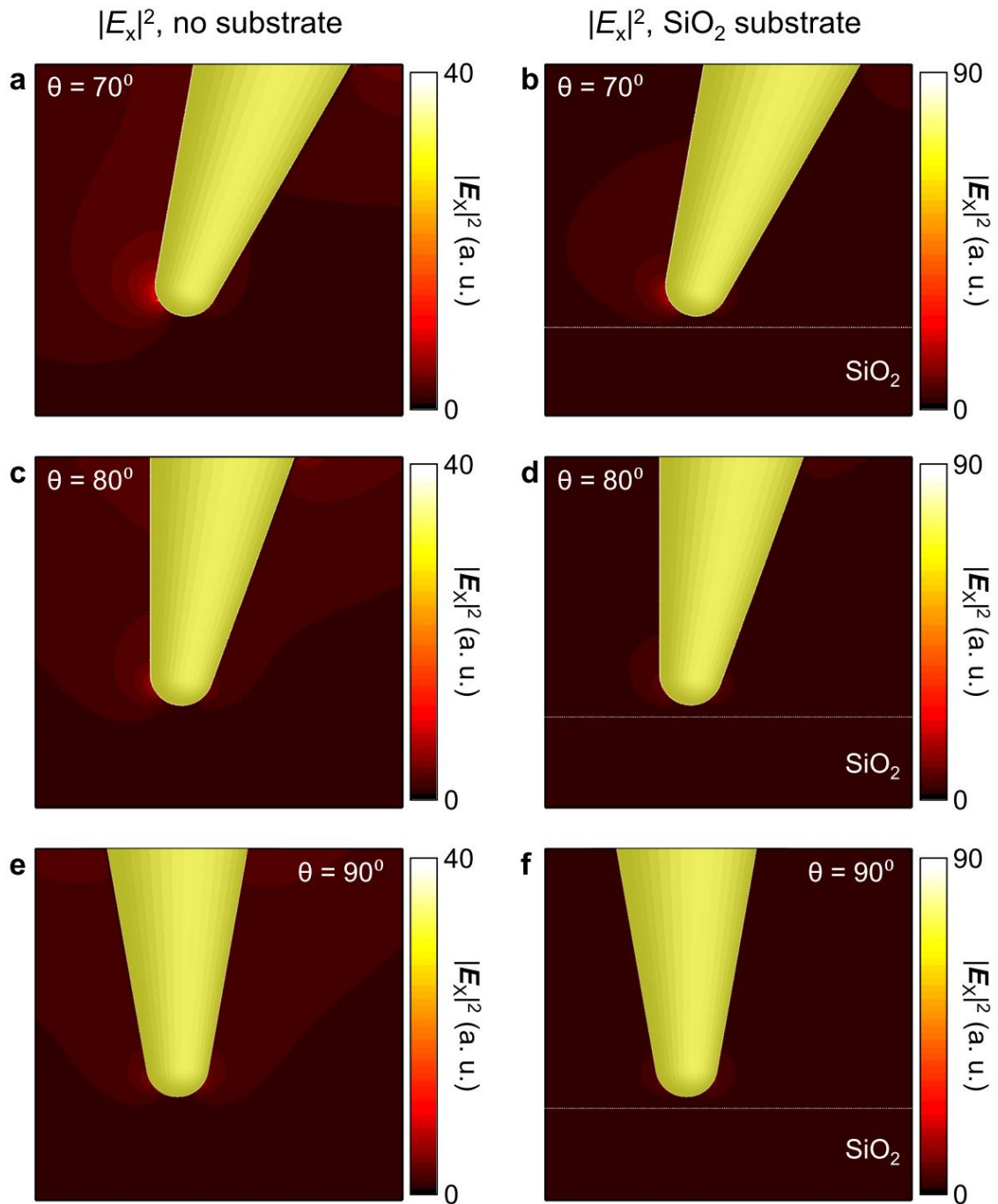d θ = 80⁰ ... 90 ... SiO₂ ... 0

f θ = 90⁰ ... 90 ... SiO₂ ... 0

Figure S7: Simulated *in-plane* optical field intensity ($|E_x|^2$) maps with respect to the tip tilt angle. (a, c, e) $|E_x|^2$ for the free standing tip (without substrate). (b, d, f) $|E_x|^2$ for the tip near the SiO₂ substrate.
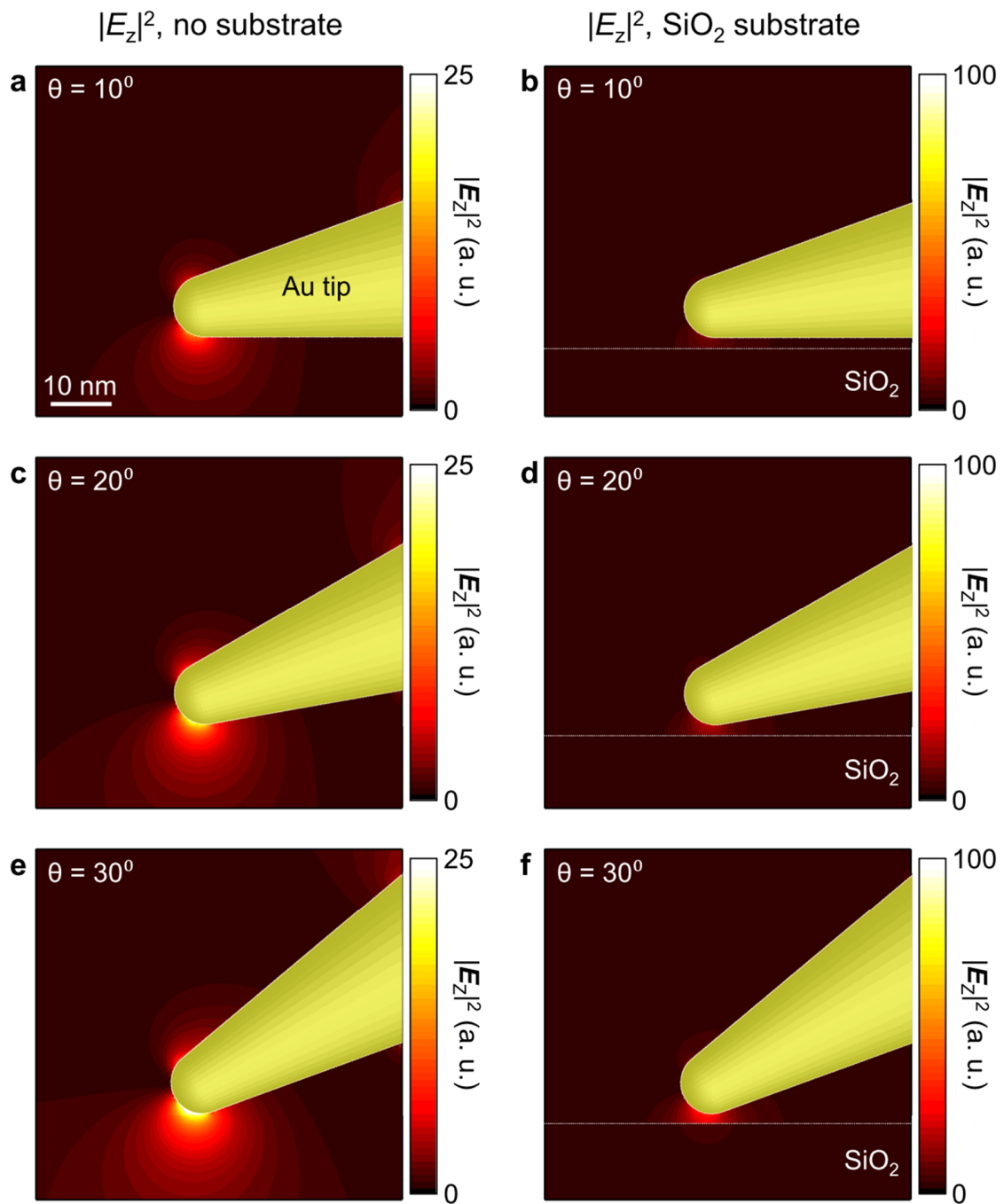
Figure S8: Simulated *out-of-plane* electric field intensity ($|E_z|^2$) maps with respect to the tip tilt angle. (a, c, e) $|E_z|^2$ for the free standing tip (without substrate). (b, d, f) $|E_z|^2$ for the tip near the SiO$_2$ substrate.

Figure S9: Simulated *out-of-plane* electric field intensity ($|E_z|^2$) maps with respect to the tip tilt angle. (a, c, e) $|E_z|^2$ for the free standing tip (without substrate). (b, d, f) $|E_z|^2$ for the tip near the SiO$_2$ substrate.
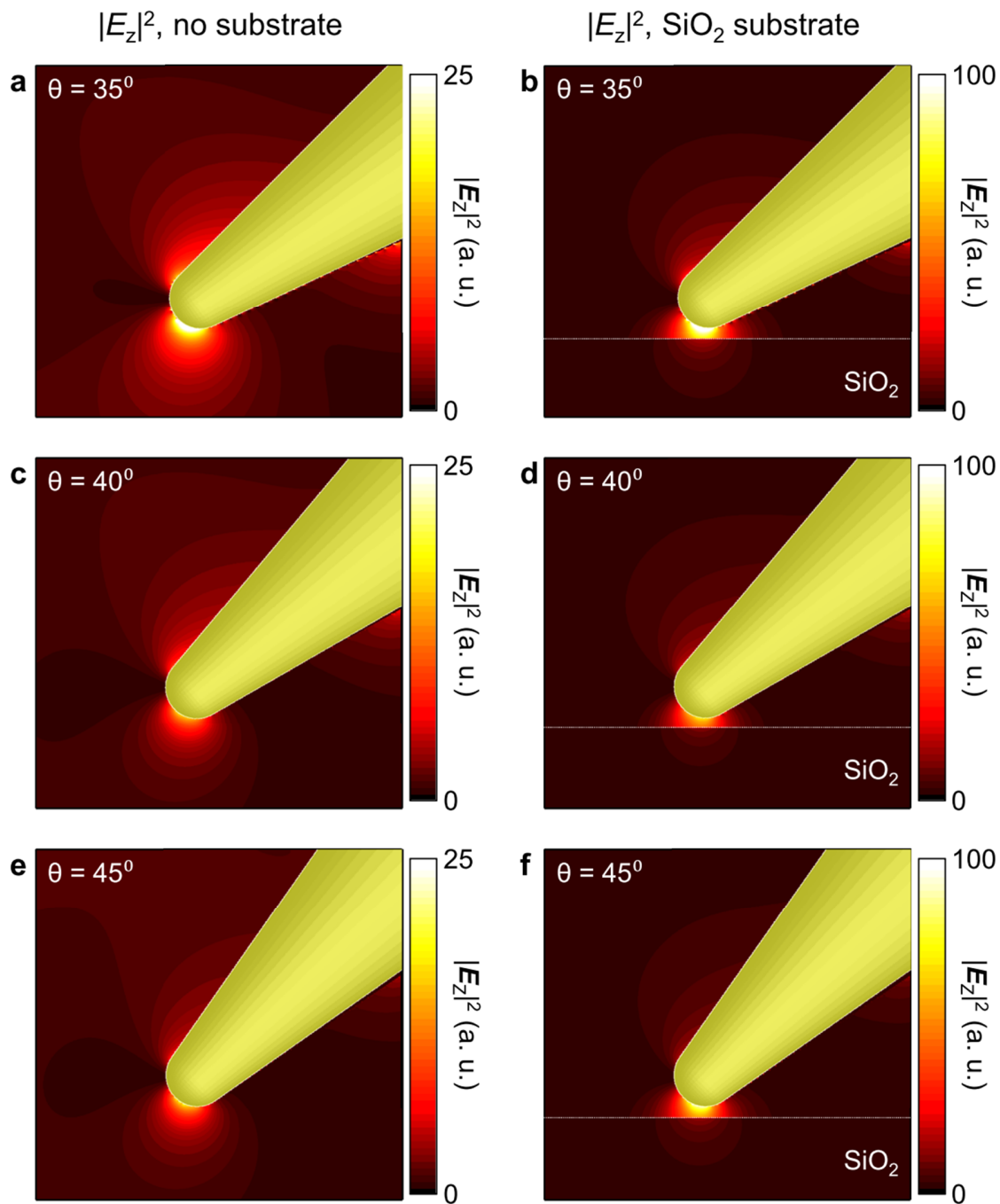
Figure S10: Simulated *out-of-plane* electric field intensity ($|E_z|^2$) maps with respect to the tip tilt angle. (a, c, e) $|E_z|^2$ for the free standing tip (without substrate). (b, d, f) $|E_z|^2$ for the tip near the SiO_2 substrate.
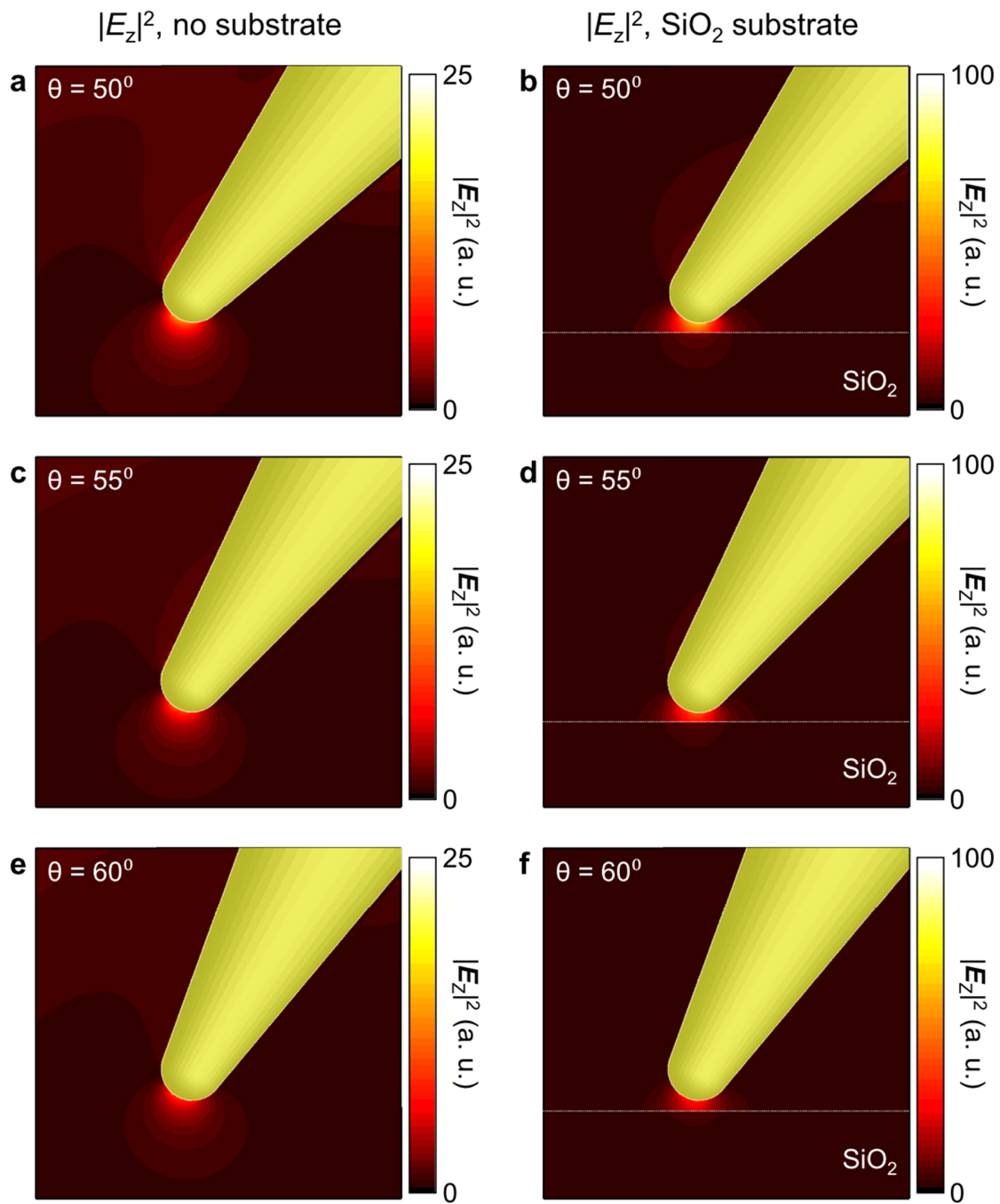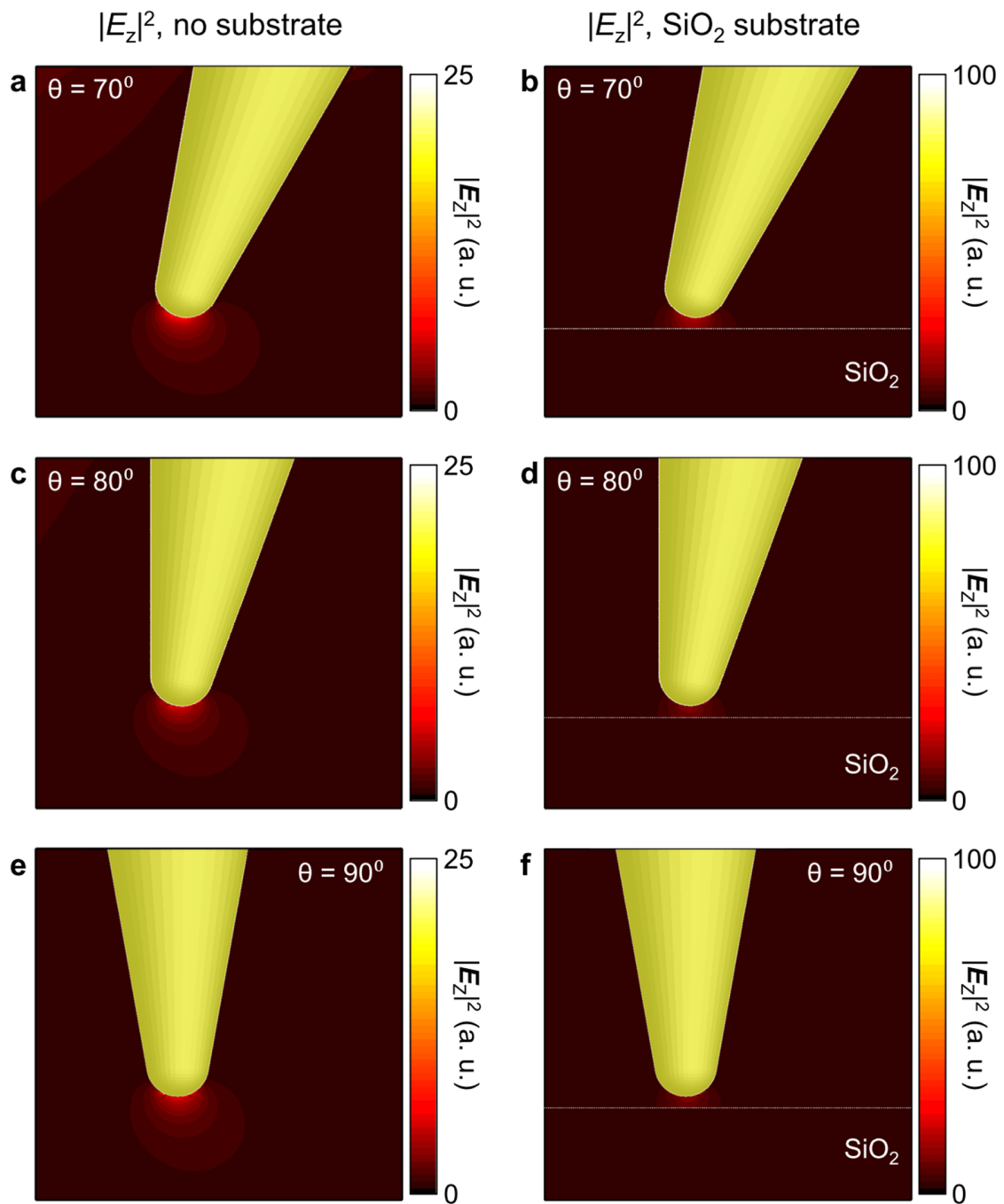
Figure S11: Simulated *out-of-plane* electric field intensity ($|E_z|^2$) maps with respect to the tip tilt angle. (a, c, e) $|E_z|^2$ for the free standing tip (without substrate). (b, d, f) $|E_z|^2$ for the tip near the SiO_2 substrate.

Selection rules for second-harmonic generation response of a monolayer MoS₂ and a single-crystalline x-cut YMnO₃ crystal

For the MoS₂ crystals with θ_{co} = 0° (C1 of Figure 4b-c), the induced second order polarization can be written as

$$\boldsymbol{P}(2\omega) = 2\epsilon_0 \chi_{ijk}^{(2)} \boldsymbol{E}_z(\omega) \boldsymbol{E}_y(\omega) \tag{1}$$

where $\boldsymbol{E}_{i=x,y,z}(\omega)$ are the electric field components at the laser frequency. Using the nonvanishing $\chi_{ijk}^{(2)}$ tensor elements for the $\bar{6}m2$ symmetry class, $\boldsymbol{P}(2\omega)$ is given by

$$\begin{bmatrix} P_x(2\omega) \\ P_y(2\omega) \\ P_z(2\omega) \end{bmatrix} = 2\epsilon_0 \begin{bmatrix} 0 & 0 & 0 & 0 & 0 & -\chi_{xxy}^{(2)} \\ -\chi_{yxx}^{(2)} & \chi_{yyy}^{(2)} & 0 & 0 & 0 & 0 \\ 0 & 0 & 0 & 0 & 0 & 0 \end{bmatrix} \begin{bmatrix} 0 \\ E_y(\omega)^2 \\ E_z(\omega)^2 \\ 2E_y(\omega)E_z(\omega) \\ 0 \\ 0 \end{bmatrix}, \tag{2}$$

$$\boldsymbol{P}_y(2\omega) = 2\epsilon_0 \chi_{yyy}^{(2)} \boldsymbol{E}_y(\omega)^2. \tag{3}$$

Therefore, the second-harmonic signal (2ω) of crystal C1 is polarized parallel to the excitation polarization (ω).

In case of the MoS₂ crystals with θ_{co} = 90° (C2 of Figure 4b-c), $\boldsymbol{P}(2\omega)$ is given by

$$\begin{bmatrix} P_x(2\omega) \\ P_y(2\omega) \\ P_z(2\omega) \end{bmatrix} = 2\epsilon_0 \begin{bmatrix} 0 & 0 & 0 & 0 & 0 & -\chi_{xxy}^{(2)} \\ -\chi_{yxx}^{(2)} & \chi_{yyy}^{(2)} & 0 & 0 & 0 & 0 \\ 0 & 0 & 0 & 0 & 0 & 0 \end{bmatrix} \begin{bmatrix} E_x(\omega)^2 \\ 0 \\ E_z(\omega)^2 \\ 0 \\ 2E_x(\omega)E_z(\omega) \\ 0 \end{bmatrix}, \tag{4}$$

$$\boldsymbol{P}_y(2\omega) = -2\epsilon_0 \chi_{yxx}^{(2)} \boldsymbol{E}_x(\omega)^2. \tag{5}$$

Therefore, the second-harmonic signal (2ω) of crystal C2 is polarized perpendicular to the excitation polarization (ω).

For the single-crystalline x-cut YMnO$_3$ (Figure 5a), the induced second order polarization can be written as

$$\boldsymbol{P}(2\omega) = 2\epsilon_0 \chi_{ijk}^{(2)} \boldsymbol{E}_x(\omega)\boldsymbol{E}_y(\omega). \tag{6}$$

Using the nonvanishing $\chi_{ijk}^{(2)}$ tensor elements for the $6m\,m$ symmetry class, $\boldsymbol{P}(2\omega)$ is given by

$$\begin{bmatrix} \boldsymbol{P}_x(2\omega) \\ \boldsymbol{P}_y(2\omega) \\ \boldsymbol{P}_z(2\omega) \end{bmatrix} = 2\epsilon_0 \begin{bmatrix} 0 & 0 & 0 & 0 & \chi_{xxz}^{(2)} & 0 \\ 0 & 0 & 0 & \chi_{yyz}^{(2)} & 0 & 0 \\ \chi_{zxx}^{(2)} & \chi_{zyy}^{(2)} & \chi_{zzz}^{(2)} & 0 & 0 & 0 \end{bmatrix} \begin{bmatrix} \boldsymbol{E}_x(\omega)^2 \\ \boldsymbol{E}_y(\omega)^2 \\ 0 \\ 0 \\ 0 \\ 2\boldsymbol{E}_x(\omega)\boldsymbol{E}_y(\omega) \end{bmatrix}, \tag{7}$$

$$\boldsymbol{P}_z(2\omega) = 2\epsilon_0 \chi_{zxx}^{(2)} (\boldsymbol{E}_x(\omega)^2 + \boldsymbol{E}_y(\omega)^2). \tag{8}$$

Therefore, the second-harmonic signal (2ω) is polarized perpendicular to the excitation polarization (ω).

Tip-enhanced SHG nano-crystallography image of monolayer MoS$_2$ film
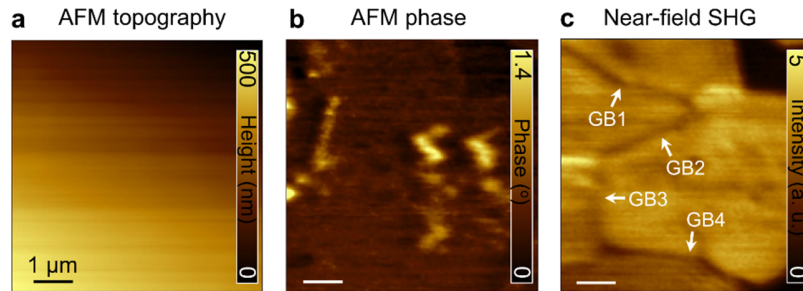

Figure S12: AFM topography, AFM phase, and tip-enhanced SHG nano-crystallography image of monolayer MoS$_2$ film on a SiO$_2$ substrate. (c) is the same image as Figure 4f in the main text. The observed contrast in AFM phase image is the chemical residue on the nucleation site in CVD growth.